

Excitation of Multi-periodic Kink Motions in Solar Flare Loops: Possible Application to Quasi-periodic Pulsations

MIJIE SHI,¹ BO LI,¹ SHAO-XIA CHEN,¹ MINGZHE GUO,^{1,2} AND SHENGJU YUAN³

¹*Shandong Key Laboratory of Optical Astronomy and Solar-Terrestrial Environment, School of Space Science and Physics, Institute of Space Sciences, Shandong University, Weihai, Shandong, 264209, China*

²*Centre for mathematical Plasma Astrophysics, Department of Mathematics, KU Leuven, 3001 Leuven, Belgium*

³*Institute of Frontier and Interdisciplinary Science, Shandong University, Qingdao, Shandong, 266237, China*

(Received; Revised; Accepted)

ABSTRACT

Magnetohydrodynamic (MHD) waves are often invoked to interpret quasi-periodic pulsations (QPPs) in solar flares. We study the response of a straight flare loop to a kink-like velocity perturbation using three-dimensional MHD simulations and forward model the microwave emissions using the fast gyrosynchrotron code. Kink motions with two periodicities are simultaneously generated, with the long-period component ($P_L = 57$ s) being attributed to the radial fundamental kink mode and the short-period component ($P_S = 5.8$ s) to the first leaky kink mode. Forward modeling results show that the two-periodic oscillations are detectable in the microwave intensities for some lines of sight. Increasing the beam size to $(1'')^2$ does not wipe out the microwave oscillations. We propose that the first leaky kink mode is a promising candidate mechanism to account for short-period QPPs. Radio telescopes with high spatial resolutions can

help distinguish between this new mechanism with such customary interpretations as sausage modes.

1. INTRODUCTION

Quasi-periodic pulsations (QPPs) are oscillatory intensity variations commonly observed in solar flare emissions across a broad range of passbands (e.g., Tan et al. 2010; Kupriyanova et al. 2010; Van Doorselaere et al. 2011; Kolotkov et al. 2015; Li et al. 2021). The typical periods of QPPs range from a fraction of a second to several minutes. A variety of candidate mechanisms have been proposed to explain QPPs (see reviews, e.g., Nakariakov & Melnikov 2009; Van Doorselaere et al. 2016; McLaughlin et al. 2018; Kupriyanova et al. 2020; Zimovets et al. 2021). However, the physical mechanisms responsible for generating QPPs remain uncertain.

Rapid QPPs, namely those QPPs with periodicities on the order of seconds, are customarily attributed to such mechanisms as oscillatory reconnection (e.g., Craig & McClymont 1991; Hassam 1992) or sausage modes (e.g., Roberts et al. 1983; Nakariakov et al. 2003). Oscillatory reconnection can occur at a two-dimensional X-point as a consequence of, say, the impingement by velocity pulses (McLaughlin et al. 2009). This mechanism was shown to operate in the hot corona with the oscillatory periods independent of the initial velocity pulse (Karampelas et al. 2022). Sausage modes can cause periodic compression and rarefaction and thus modulate the microwave emissions of flare loops (e.g., Mossessian & Fleishman 2012; Reznikova et al. 2014; Kuznetsov et al. 2015; Guo et al. 2021; Kupriyanova et al. 2022; Shi et al. 2022). Candidate sausage modes have been reported in observations of QPPs in various passbands (e.g., Melnikov et al. 2005; Zimovets & Struminsky 2010; Su et al. 2012; Kolotkov et al. 2015; Tian et al. 2016; see the recent review by Li et al. 2020).

QPPs with multiple periodicities are often observed (Tan et al. 2010). Magnetohydrodynamic (MHD) waves are accepted to play an important role for the formation of these multi-periodic signals. Inglis & Nakariakov (2009) interpreted their multi-periodic event as the result of kink-mode-triggered magnetic reconnection. Multiple periodic QPPs can also be attributed to the superposition of different modes, for example, fast and slow sausage modes (Van Doorselaere et al. 2011), axial

fundamental kink mode and its axial overtones (Kupriyanova et al. 2013), kink mode and sausage mode (Kolotkov et al. 2015). In these studies, the long-period (several tens of seconds) signals are often attributed to kink or slow sausage modes, whereas the short-period (several seconds) signals to fast sausage modes.

In this work, we simulate kink motions in flare loops and forward model their microwave signatures, examining the possibility that both short- and long-period kink motions can be excited simultaneously. We present the MHD setup and results in Section 2, moving on to describe the forward modeling setup and results in Section 3. Section 4 summarizes this study.

2. MHD SIMULATION

2.1. Numerical Setup

We model flare loops as field aligned, z -directed, axially uniform cylinders. The equilibrium density distribution is prescribed by

$$\rho = \rho_e + (\rho_i - \rho_e)f(r), \quad (1)$$

where $[\rho_i, \rho_e] = [4 \times 10^{10}, 1 \times 10^9] m_p \text{ cm}^{-3}$ represent the internal and external mass densities. In addition, m_p is the proton mass. By ‘internal’ (subscript i) and ‘external’ (subscript e), we refer to the equilibrium quantities at the loop axis and far from the loop, respectively. A continuous profile $f(r) = \exp[-(r/R)^\alpha]$ is used to connect ρ_i and ρ_e , with $r = \sqrt{x^2 + y^2}$, $\alpha = 15$, and the nominal loop radius $R = 3 \text{ Mm}$. The temperature distribution follows the same spatial dependence as the density, with $[T_i, T_e] = [10, 2] \text{ MK}$. The magnetic field \mathbf{B} is z -directed, its magnitude varying from $B_i = 60 \text{ G}$ to $B_e = 80 \text{ G}$ to maintain transverse force balance. The pertinent Alfvén speeds are $[v_{Ai}, v_{Ae}] = [654, 5510] \text{ km s}^{-1}$. The loop length is $L_0 = 30 \text{ Mm}$. The specification of our equilibrium is largely in accordance with typical measurements (e.g., Tian et al. 2016). Figure 1 shows the initial density distributions in the $z = L_0/2$ and $x = 0$ cuts. The equilibrium is perturbed by a kink-like initial velocity perturbation in the x -direction

$$v_x(x, y, z; t = 0) = v_0 \exp\left(-\frac{r^2}{2\sigma^2}\right) \sin\left(\frac{\pi z}{L_0}\right), \quad (2)$$

where $v_0 = 20 \text{ km s}^{-1}$ is the amplitude, and $\sigma = R$ characterizes the spatial extent ¹.

The set of ideal MHD equations is evolved using the finite-volume code PLUTO (Mignone et al. 2007). We use the piecewise parabolic method for spatial reconstruction, and the second-order Runge–Kutta method for time-stepping. The HLLD approximate Riemann solver is used for computing inter-cell fluxes, and a hyperbolic divergence cleaning method is used to keep the magnetic field divergence-free. The simulation domain is $[-15, 15] \text{ Mm} \times [-15, 15] \text{ Mm} \times [0, 30] \text{ Mm}$. A uniform grids with cell numbers of $[N_x, N_y, N_z] = [1000, 1000, 100]$ is adopted. We use the outflow boundary condition for all primitive variables at the lateral boundaries (x and y). For the top and bottom boundaries (z), the transverse velocities (v_x and v_y) are fixed at zero. The density, pressure, and B_z are fixed at their initial values. The other variables are set as outflow. Our numerical results vary little when, say, a finer grid or a larger domain is experimented with. In particular, no spurious reflection is discernible at the lateral boundaries.

2.2. Numerical Results

Figure 2 displays the temporal evolution of v_x sampled at the loop center $(x, y, z) = (0, 0, L_0/2)$. One sees that two periodicities co-exist. We decompose the time sequence into a long-period (the red curve) and a short-period (green) component. This decomposition is performed using the low-(high-) pass filter of the *filtfilt* function in the *SciPy* package, with the threshold period chosen to be 10 s. The periods of the two components are $P_L = 57 \text{ s}$ and $P_S = 5.8 \text{ s}$, respectively. Both components are seen to experience temporal damping.

The snapshot at $t = 116 \text{ s}$ of the density at the loop apex is displayed in Figure 3(a). Some rolled-up vortices can be readily seen at the loop boundary close to the y -axis, suggesting the development of the Kelvin-Helmholtz instability as a result of localized shearing motions (e.g., Terradas et al. 2008; Soler et al. 2010; Antolin et al. 2015). Figure 3(b) shows the velocity field at the loop apex, together with its low-pass (Figure 3(c)) and high-pass (Figure 3(d)) components. Figure 3(e) further displays the temporal evolution of $v_x(x, y = 0, z = L_0/2; t)$. The multi-periodic oscillation is clearly

¹ The effect of σ is also worth examining. The results are collected in Appendix B to streamline the main text.

shown in the loop interior. The period of $P_L = 57$ s is consistent with that of the radial fundamental kink mode. The low-pass component of the velocity field (Figure 3(c) and the related animation) is typical of a radial fundamental kink mode as well (e.g., Goossens et al. 2014). Therefore, the long-period oscillation is identified as the radial fundamental kink mode. This identification is further corroborated by a comparison with independent theoretical expectations from an eigenvalue problem perspective in Appendix A.1, where we show that the associated temporal damping is attributable to resonant absorption (Goossens et al. 2011).

The short-period component ($P_S = 5.8$ s) shows up as ridge-like structures crossing each other in the loop interior shown in Figure 3(e). The slope of each ridge matches the fast speed in the loop interior, indicating a fast wave nature of these ridges. The high-pass component of the velocity field (Figure 3(d) and the related animation) shows some rapid variation of a dipole-like velocity field at the loop interior. These features are consistent with the first leaky kink mode, i.e., the extension to the leaky regime of the first radial overtone with the damping attributable to lateral leakage (e.g., Spruit 1982; Cally 1986, 2003). The short-period oscillation associated with a first leaky kink mode is of particular interest as it has not been invoked for interpreting QPPs to our knowledge. Our numerical results show that the first leaky kink mode can be generated along with the radial fundamental kink mode and this scenario is likely to happen in flare loops. On this aspect we stress that the associated velocity field has not been demonstrated in initial value problem studies (see Appendix A.2 for further discussions).

3. FORWARD MODELING THE GYROSYNCHROTRON EMISSION

3.1. Method

We compute gyrosynchrotron (GS) emissions using the fast GS code (Kuznetsov et al. 2011; Fleishman & Kuznetsov 2010). The fast GS code computes the local values of the absorption coefficient and emissivity, thereby accounting for inhomogeneous sources by integrating the radiative transfer equation. We assume that non-thermal electrons occupy a time-varying volume that initially corresponds to $r \leq 2$ Mm (the yellow volume in Figure 1). This assumption is based on the consideration

that the non-thermal electrons determined by some acceleration mechanism may fill only part of the loop, similar to the model used in Kupriyanova et al. (2022). This volume moves back and forth due to the kink motions. We trace this volume using a passive scaler as the simulation goes on. Within this volume, we further assume that the number density (N_b) of the non-thermal electrons is proportional to the thermal one (N_e), and specifically takes the form $N_b = 0.005N_e$. The spectral index of the non-thermal electrons is $\delta = 3$, with the energy ranging from 0.1 to 10 MeV. The pitch angle distribution of the non-thermal electrons is taken to be isotropic. We assume that any line of sight (LoS) is located in the $y - z$ plane, making an angle of 45° with both the y - and z -axis. The LoS intersects the apex plane $z = L_0/2$ at (x_0, y_0) and threads a beam with a cross-sectional area of $60 \text{ km} \times 60 \text{ km}$. We select three beams with different x_0 (i.e., $x_0 = 0, \pm 1 \text{ Mm}$) by adopting a fixed $y_0 = 0$. The white line in Figure 1 illustrates the LoS for the case $x_0 = 0 \text{ Mm}$.

3.2. Results

We forward model the GS emission and examine the microwave signature of the kink motions, taking the 17 GHz emission as an example. Figure 4(a) shows the intensity variations for the three beams ($x_0 = 0, \pm 1 \text{ Mm}$). One sees that the intensity variation is negligible for the beam that passes through the loop axis ($x_0 = 0$). However, the intensity shows obvious variations with two different periodicities for the rest of the beams ($x_0 = \pm 1 \text{ Mm}$). We decompose the intensity variations into a long-period (Figure 4(b)) and a short-period (Figure 4(c)) component for the cases $x_0 = \pm 1 \text{ Mm}$. The periods of the two components are consistent with P_L and P_S , meaning that the two periodicities of the microwave intensity are the manifestations of the simultaneously excited radial fundamental kink mode and the first leaky kink mode. We also find that the intensity variations are anti-correlated between the cases $x_0 = 1 \text{ Mm}$ and $x_0 = -1 \text{ Mm}$. This behavior is caused by the asymmetric variations between the left and right sides of the loop for the two modes.

Figure 5(a) shows the intensity variations for the case $x_0 = 1 \text{ Mm}$ when different beam sizes are adopted. The intensity of a larger beam is achieved by adding the intensity of all single beams in the corresponding area projected onto the plane of sky. Figures 5(b) and 5(c) display the low-pass and high-pass component. One sees that increasing the beam size to as large as $(1'')^2$ does not change the

two-periodicity behavior of the microwave intensities. For the short-period component, the intensity variations are almost the same for different beam sizes.

The kink motions with two periodicities are likely to be detectable using modern radio telescopes. The Mingantu Spectral Radioheliograph (MUSER, [Yan et al. \(2021\)](#)) observes the Sun with a time cadence of 0.2 s and a spatial resolution of 1.3'' at 15 GHz. The Atacama Large Millimeter/submillimeter Array (ALMA, [Wedemeyer et al. \(2016\)](#)) can achieve unprecedented high resolutions at 85 GHz.

4. SUMMARY

We examined the response of a straight flare loop to a kink-like initial velocity perturbation using 3D MHD simulations. We found that kink motions with two periodicities are simultaneously generated in the loop interior. The long-period component ($P_L = 57$ s) is attributed to the radial fundamental kink mode, and the short-period component ($P_S = 5.8$ s) to the first leaky kink mode. We then examined the modulation of the microwave intensity by the kink motions via forward modeling the GS emissions. We found that the two-periodic signals are detectable in the 17 GHz microwave emission at some LoS directions. Increasing the beam size to as large as $(1'')^2$ does not wipe out these oscillatory signals.

Leaky kink modes are a promising candidate mechanism to account for short-period QPPs in flare loops. [Kolotkov et al. \(2015\)](#) detected multi-periodic QPPs and interpreted the long-period component (100 s) as a radial fundamental kink mode and the short-period component (15 s) as a sausage mode. We argue that the short-period component in their observations can be alternatively interpreted as the first leaky kink mode. However, we cannot distinguish between the two mechanisms based purely on the oscillation period, because the timescales of the first leaky kink modes and sausage modes are close. Radio telescopes with high spatial resolutions would be very helpful to identify the first leaky kink modes. For sausage modes, the intensity variations are expected to be in-phase across the entire loop, whereas for the first leaky kink modes the intensity variations are anti-correlated between the left and right sides of the loop.

1 We thank the referee for constructive comments. This work is supported by the National Natural
 2 Science Foundation of China (41904150, 12273019, 41974200, 11761141002, 12203030). We gratefully
 3 acknowledge ISSI-BJ for supporting the international team “Magnetohydrodynamic wavetrains as a
 4 tool for probing the solar corona ”.

APPENDIX

A. COMPARISON BETWEEN 3D TIME-DEPENDENT RESULTS AND THEORETICAL EXPECTATIONS

The temporal evolution of v_x at three different locations in the apex plane ($z = L_0/2$) is displayed by the blue curves in the left column of Figure 6. Two periodicities can be readily seen in any time sequence, which is therefore decomposed into a long-period (the red curves) and a short-period (green) component. We then fit both components using an exponentially damping sinusoid $A_0 \sin(2\pi t/P + \phi_0) \exp(-t/\tau)$, printing the best-fit periods ($P_{L,S}$) and damping times ($\tau_{L,S}$) on each plot. The best-fit curves are additionally displayed by the black dotted lines.

A.1. *the Long-period Component*

The radial fundamental kink mode is well known to be resonantly absorbed in the Alfvén continuum in a radially continuous equilibrium with our ordering of the characteristic speeds (e.g., Goossens et al. 2011). However, one complication is that our radial profile (see Equation (1)) is not readily amenable to analytical treatment. We therefore proceed with the numerical approach in Chen et al. (2021), computing the radial fundamental kink mode as a resistive eigenmode (see Goossens et al. 2011, for conceptual clarifications). The code outputs a period of $P_L^{\text{EVP}} = 57.3$ s and a damping time of $\tau_L^{\text{EVP}} = 107$ s, where the superscript indicates that these expectations are derived from an eigenvalue problem (EVP) perspective ². One sees that the expected period and damping time agree

² The period of the radial fundamental kink mode reads $2L_0/c_k \approx 55.8$ s in the thin-tube (TT) thin-boundary (TB) limit, with c_k being the kink speed (e.g., Goossens et al. 2011). This is not far from P_L^{EVP} . We refrain from comparing τ_L^{EVP} with the TTTB expectation, because an expression is not available for our radial profile. The detailed formulation of a radial profile, however, is known to impact the TTTB expectations for the damping time (e.g., Soler et al. 2014).

remarkably well with the best-fit values that we derive with the 3D time-dependent simulation (the left column of Figure 6).

A.2. the Short-period Component

This subsection compares our short-period component with the EVP expectations for the first leaky kink mode. We restrict ourselves to the piecewise constant version (i.e., $\alpha \rightarrow \infty$) of our equilibrium. The pertinent flow field is emphasized, despite that the expressions we offer are not new per se (e.g., Cally 1986, 2003). We work in a cylindrical coordinate system (r, θ, z) , denoting the equilibrium quantities with the subscript 0. The interior and exterior are further discriminated by the subscripts i and e. There appears a set of primitive quantities $\{\rho_{i,e}, p_{i,e}, B_{i,e}\}$, where ρ , p , and B represent the mass density, thermal pressure, and magnetic field strength, respectively. We define the Alfvén (v_A), adiabatic sound (c_s), and tube speeds (c_T) as

$$v_{\text{Ai,e}}^2 = \frac{B_{i,e}^2}{\mu_0 \rho_{i,e}}, \quad c_{\text{si,e}}^2 = \frac{\gamma p_{i,e}}{\rho_{i,e}}, \quad c_{\text{Ti,e}}^2 = \frac{v_{\text{Ai,e}}^2 c_{\text{si,e}}^2}{v_{\text{Ai,e}}^2 + c_{\text{si,e}}^2}, \quad (\text{A1})$$

with μ_0 the magnetic permeability of free space and $\gamma = 5/3$ the ratio of specific heats.

Our EVP expectations are as follows. With kink motions in mind, we write any small-amplitude perturbation δg as

$$\delta g(r, \theta, z; t) = \Re \{ \tilde{g}(r) \exp[-i(\omega t - kz - \theta)] \}, \quad (\text{A2})$$

where k denotes the real-valued axial wavenumber, and $\omega = \omega_R + i\omega_I$ represents the angular frequency.

Only temporally non-growing solutions are sought ($\omega_I \leq 0$). Defining

$$\mu_{i,e}^2 = \frac{(\omega^2 - k^2 v_{\text{Ai,e}}^2)(\omega^2 - k^2 c_{\text{si,e}}^2)}{(v_{\text{Ai,e}}^2 + c_{\text{si,e}}^2)(\omega^2 - k^2 c_{\text{Ti,e}}^2)}, \quad (\text{A3})$$

we further take $\omega_R > 0$ and $-\pi/2 < \arg \mu_{i,e} \leq \pi/2$. A dispersion relation (DR) then writes

$$\frac{\mu_i R}{\omega^2 - k^2 v_{\text{Ai}}^2} \frac{J_1'(\mu_i R)}{J_1(\mu_i R)} = \frac{\rho_i}{\rho_e} \frac{\mu_e R}{\omega^2 - k^2 v_{\text{Ae}}^2} \frac{(H_1^{(1)})'(\mu_e R)}{H_1^{(1)}(\mu_e R)}, \quad (\text{A4})$$

which accounts for both the trapped and leaky regimes. Here J_n ($H_n^{(1)}$) denotes the Bessel (Hankel) function of the first kind (with $n = 1$). The prime $'$ represents, say, $dJ_1(\mathfrak{z})/d\mathfrak{z}$ with \mathfrak{z} evaluated at

$\mu_i R$. Standard procedure further yields that

$$\tilde{p}_T(r) = \frac{B_i^2}{\mu_0} \times \begin{cases} J_1(\mu_i r)/J_1(\mu_i R), & 0 \leq r \leq R, \\ H_1^{(1)}(\mu_e r)/H_1^{(1)}(\mu_e R), & r \geq R, \end{cases} \quad (\text{A5})$$

where the arbitrarily scaled \tilde{p}_T denotes the Fourier amplitude of the total pressure perturbation. For both the interior and exterior, the Fourier amplitudes for the radial and azimuthal speeds write

$$\tilde{v}_r(r) = \frac{-i\omega}{\rho_0(\omega^2 - k^2 v_A^2)} \frac{d\tilde{p}_T}{dr}, \quad (\text{A6})$$

$$\tilde{v}_\theta(r) = \frac{\omega}{\rho_0(\omega^2 - k^2 v_A^2)} \frac{\tilde{p}_T}{r}. \quad (\text{A7})$$

Our EVP expectations amount to time-dependent perturbations that are standing in both axial and azimuthal directions, the net results being

$$v_r(r, \theta, z; t) = A \sin(kz) \cos \theta \Re [i\tilde{v}_r(r)e^{-i\omega t}] = [A \sin(kz)e^{\omega t}] \{ \cos \theta \Re [i\tilde{v}_r(r)e^{-i\omega_R t}] \}, \quad (\text{A8})$$

$$v_\theta(r, \theta, z; t) = A \sin(kz) \sin \theta \Re [-\tilde{v}_\theta(r)e^{-i\omega t}] = [A \sin(kz)e^{\omega t}] \{ \sin \theta \Re [-\tilde{v}_\theta(r)e^{-i\omega_R t}] \}. \quad (\text{A9})$$

Here A is some arbitrary, real-valued, dimensionless magnitude.

We now compare our short-period component with the EVP expectations. To start, plugging our equilibrium quantities into Equation (A4) yields a period of $P_S^{\text{EVP}} = 5.96$ s and a damping time of $\tau_S^{\text{EVP}} = 150$ s. This pertains to the first leaky mode, namely the one that possesses the lowest ω_R among all modes with $\omega_I < 0$ ³. The expected period is in good agreement with the best-fit values printed in the left column of Figure 6. The best-fit damping times, on the other hand, are somehow shorter than expected, which is intuitively understandable because a radially discontinuous cylinder leads to more efficient wave trapping. Figure 7a further displays the velocity fields in the apex plane of our short-period component at some representative instant. Plotted in Figure 7b is the pertinent EVP expectation, namely the flow field constructed with the terms in the braces of Equations (A8) and (A9) at $\omega_R t = 0$. The two sets of flow fields are remarkably similar. Overall, we conclude that the short-period component can be confidently identified as the first leaky kink mode.

³ Some analytical expressions are available that approximately solve Equation (A4) in some appropriate limits (e.g., Cally 2003; Spruit 1982). We choose to solve Equation (A4) exactly, because the eigenfunctions are also of interest.

B. EFFECT OF VARYING σ

This section examines how the relative importance of the long- and short-period components varies when we vary the spatial extent of the initial perturbation (i.e., σ in Equation 2). Two additional simulations are performed, one with $\sigma = 0.5R$ and the other with $\sigma = 2R$. These additional computations are shown in the middle and right columns of Figure 6 in the same format as our reference results (with $\sigma = R$). Two pronounced periodicities can be readily told apart in any sampled v_x . The following features stand out for the short-period components. Firstly, their best-fit periods and damping times vary little from one case to another, indicating the robust excitation of the first leaky kink mode. Secondly, the short-period component tends to be stronger for smaller values of σ , suggesting that leaky modes can receive a larger fraction of the energy imparted by the initial perturbation when it is more localized.

Some subtlety exists for the long-period component when $\sigma = 0.5R$. Overall, the temporal behavior for v_x deviates from an exponentially damping sinusoid, in contrast to what happens for other values of σ that we examine. We refrain from explaining why at this time of writing. Rather, we note that this deviation is not a numerical artifact but persists even when we adopt a considerably larger computational domain.

REFERENCES

- | | |
|--|---|
| Antolin, P., Okamoto, T. J., De Pontieu, B., et al. 2015, <i>ApJ</i> , 809, 72 | Goossens, M., Erdélyi, R., & Ruderman, M. S. 2011, <i>SSRv</i> , 158, 289 |
| Cally, P. S. 1986, <i>SoPh</i> , 103, 277 | Goossens, M., Soler, R., Terradas, J., Van Doorselaere, T., & Verth, G. 2014, <i>ApJ</i> , 788, 9 |
| —. 2003, <i>SoPh</i> , 217, 95 | Guo, M., Li, B., & Shi, M. 2021, <i>ApJL</i> , 921, L17 |
| Chen, S.-X., Li, B., Van Doorselaere, T., et al. 2021, <i>ApJ</i> , 908, 230 | Hassam, A. B. 1992, <i>ApJ</i> , 399, 159 |
| Craig, I. J. D., & McClymont, A. N. 1991, <i>ApJL</i> , 371, L41 | Inglis, A. R., & Nakariakov, V. M. 2009, <i>A&A</i> , 493, 259 |
| Fleishman, G. D., & Kuznetsov, A. A. 2010, <i>ApJ</i> , 721, 1127 | Karampelas, K., McLaughlin, J. A., Botha, G. J. J., & Régnier, S. 2022, <i>ApJ</i> , 933, 142 |

- Kolotkov, D. Y., Nakariakov, V. M., Kupriyanova, E. G., Ratcliffe, H., & Shibasaki, K. 2015, *A&A*, 574, A53
- Kupriyanova, E., Kolotkov, D., Nakariakov, V., & Kaufman, A. 2020, *Solar-Terrestrial Physics*, 6, 3
- Kupriyanova, E. G., Kaltman, T. I., & Kuznetsov, A. A. 2022, *MNRAS*, 516, 2292
- Kupriyanova, E. G., Melnikov, V. F., Nakariakov, V. M., & Shibasaki, K. 2010, *SoPh*, 267, 329
- Kupriyanova, E. G., Melnikov, V. F., & Shibasaki, K. 2013, *SoPh*, 284, 559
- Kuznetsov, A. A., Nita, G. M., & Fleishman, G. D. 2011, *ApJ*, 742, 87
- Kuznetsov, A. A., Van Doorselaere, T., & Reznikova, V. E. 2015, *SoPh*, 290, 1173
- Li, B., Antolin, P., Guo, M. Z., et al. 2020, *SSRv*, 216, 136
- Li, D., Ge, M., Dominique, M., et al. 2021, *ApJ*, 921, 179
- McLaughlin, J. A., De Moortel, I., Hood, A. W., & Brady, C. S. 2009, *A&A*, 493, 227
- McLaughlin, J. A., Nakariakov, V. M., Dominique, M., Jelínek, P., & Takasao, S. 2018, *SSRv*, 214, 45
- Melnikov, V. F., Reznikova, V. E., Shibasaki, K., & Nakariakov, V. M. 2005, *A&A*, 439, 727
- Mignone, A., Bodo, G., Massaglia, S., et al. 2007, *ApJS*, 170, 228
- Mossessian, G., & Fleishman, G. D. 2012, *ApJ*, 748, 140
- Nakariakov, V. M., & Melnikov, V. F. 2009, *SSRv*, 149, 119
- Nakariakov, V. M., Melnikov, V. F., & Reznikova, V. E. 2003, *A&A*, 412, L7
- Reznikova, V. E., Antolin, P., & Van Doorselaere, T. 2014, *ApJ*, 785, 86
- Roberts, B., Edwin, P. M., & Benz, A. O. 1983, *Nature*, 305, 688
- Shi, M., Li, B., & Guo, M. 2022, *ApJL*, 937, L25
- Soler, R., Goossens, M., Terradas, J., & Oliver, R. 2014, *ApJ*, 781, 111
- Soler, R., Terradas, J., Oliver, R., Ballester, J. L., & Goossens, M. 2010, *ApJ*, 712, 875
- Spruit, H. C. 1982, *SoPh*, 75, 3
- Su, J. T., Shen, Y. D., Liu, Y., Liu, Y., & Mao, X. J. 2012, *ApJ*, 755, 113
- Tan, B., Zhang, Y., Tan, C., & Liu, Y. 2010, *ApJ*, 723, 25
- Terradas, J., Andries, J., Goossens, M., et al. 2008, *ApJL*, 687, L115
- Tian, H., Young, P. R., Reeves, K. K., et al. 2016, *ApJL*, 823, L16
- Van Doorselaere, T., De Groof, A., Zender, J., Berghmans, D., & Goossens, M. 2011, *ApJ*, 740, 90
- Van Doorselaere, T., Kupriyanova, E. G., & Yuan, D. 2016, *SoPh*, 291, 3143
- Wedemeyer, S., Bastian, T., Brajša, R., et al. 2016, *SSRv*, 200, 1
- Yan, Y., Chen, Z., Wang, W., et al. 2021, *Frontiers in Astronomy and Space Sciences*, 8, 20

Zimovets, I. V., & Struminsky, A. B. 2010, SoPh,
263, 163

Zimovets, I. V., McLaughlin, J. A., Srivastava,
A. K., et al. 2021, SSRv, 217, 66

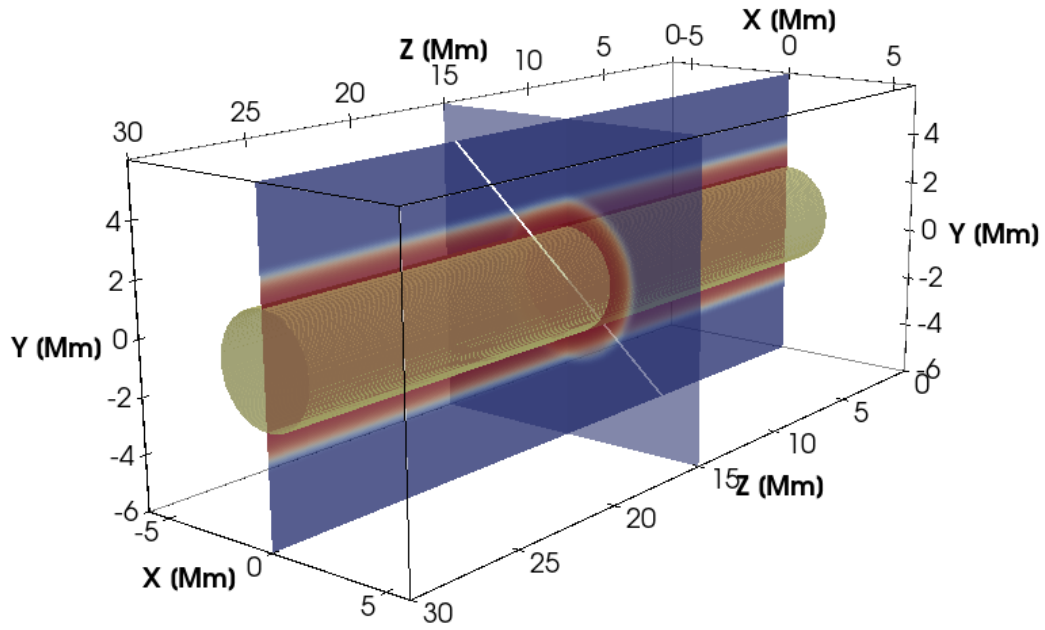


Figure 1. Initial density distributions in the $z = L_0/2$ and $x = 0$ cuts. The yellow volume shows the region where the non-thermal electrons occupy at $t = 0$. The white line marks the line of sight (LoS) for the case $x_0 = 0$.

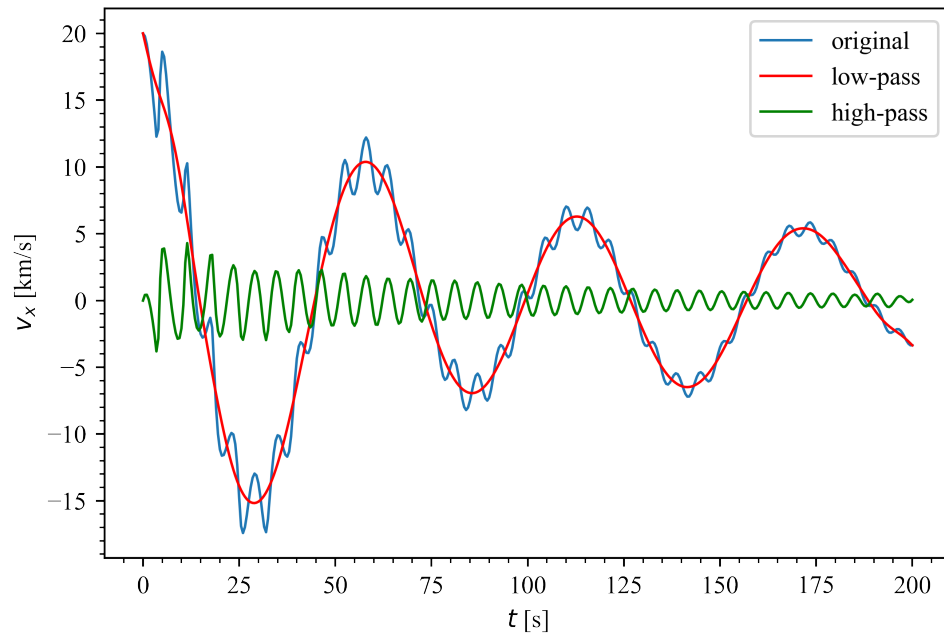


Figure 2. Temporal evolution of v_x sampled at $(x, y, z) = (0, 0, L_0/2)$ (blue), together with its low-pass (red) and high-pass (green) components.

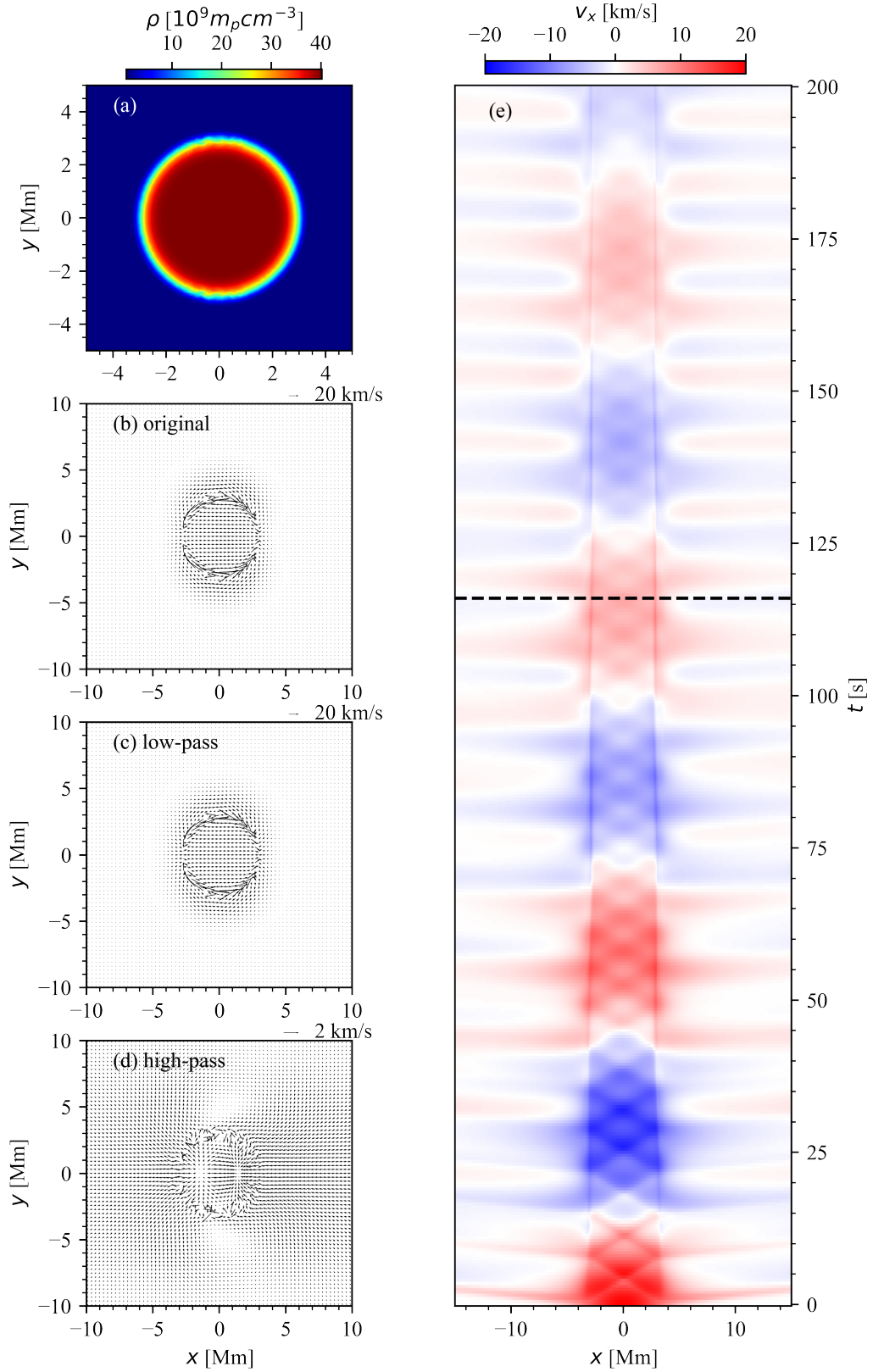


Figure 3. (a) Density distribution at the loop apex. (b) Velocity field along with its (c) long-period and (d) short-period components at the loop apex. (e) Temporal evolution of $v_x(x, y = 0, z = L_0/2)$. The black dashed line marks the instant (116 s) where the figures in the left column are produced. An animated version of this figure is available that has the same layout as the static figure, and runs from 0–200s.

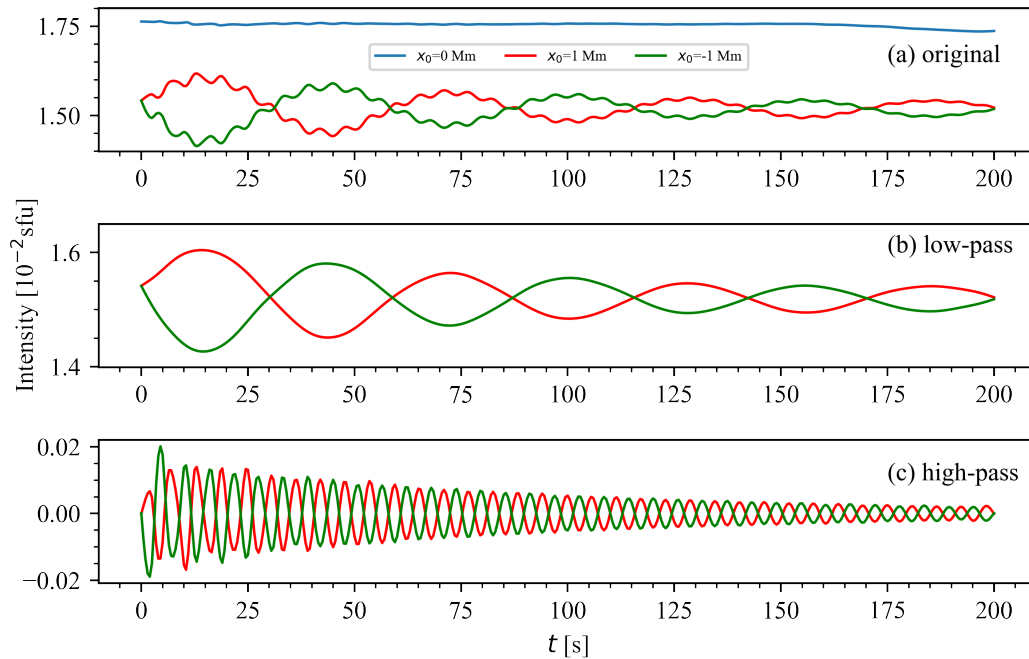


Figure 4. (a) Intensity variations of the 17 GHz emission for three LoS beams. (b) Low-pass and (c) high-pass components of the intensity variations for $x_0 = \pm 1$ Mm.

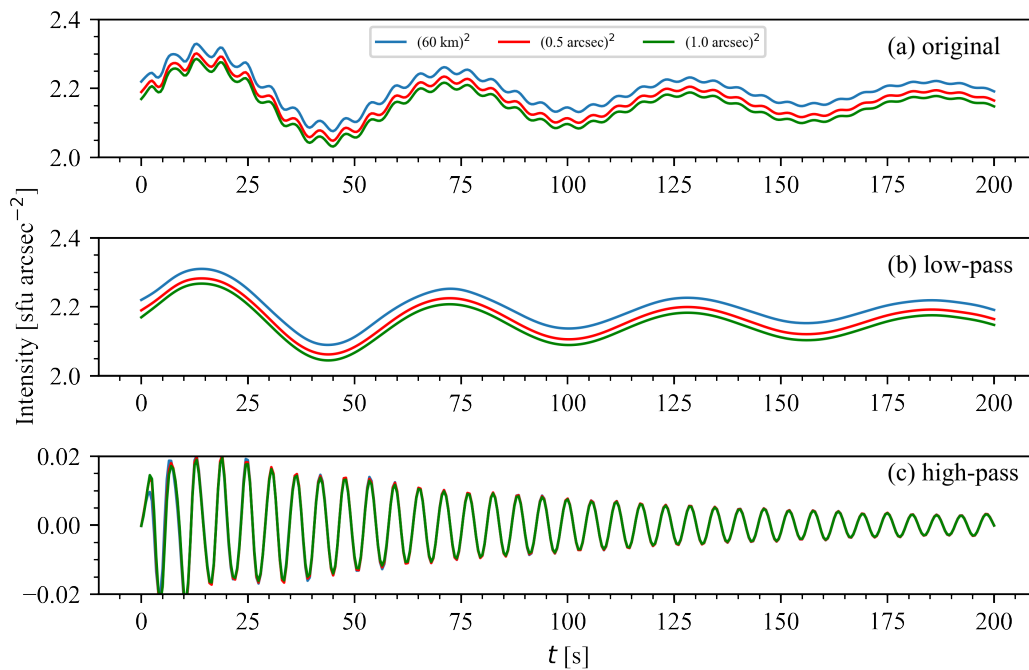


Figure 5. (a) Intensity variations of the 17 GHz emission for different beam sizes for the case $x_0 = 1$ Mm. (b) Low-pass and (c) high-pass components of (a).

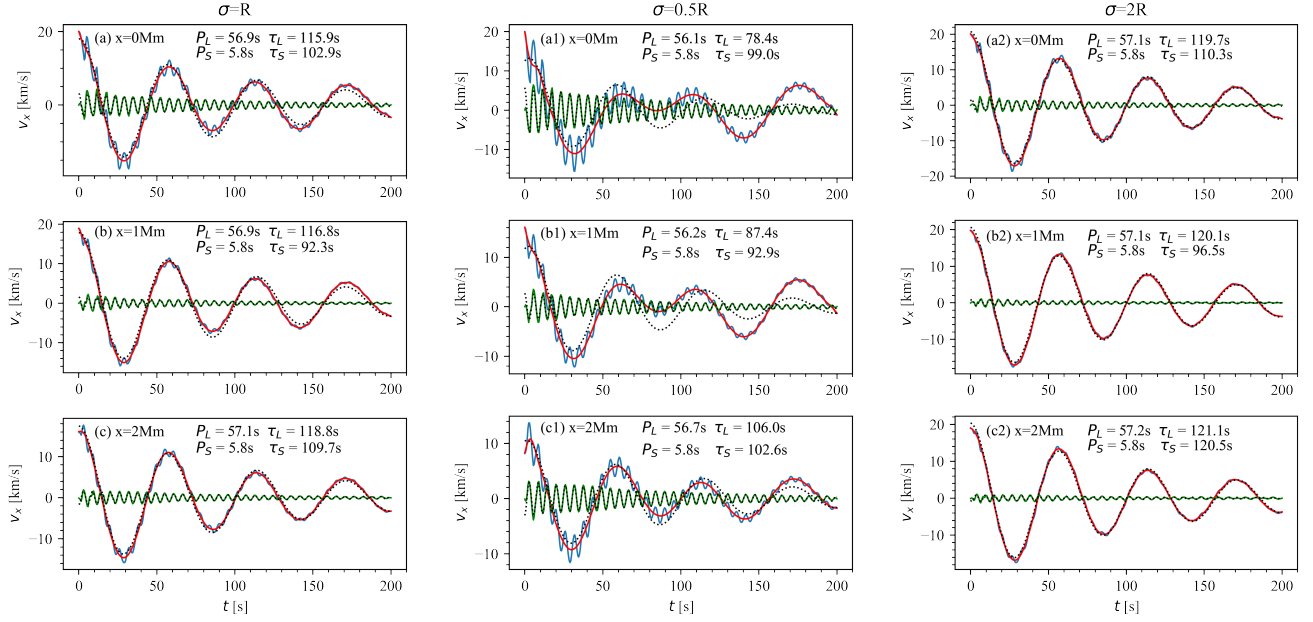


Figure 6. Left column: Temporal evolution of v_x sampled in the apex plane at (a) $(x, y) = (0, 0)\text{Mm}$, (b) $(x, y) = (1, 0)\text{Mm}$, and (c) $(x, y) = (2, 0)\text{Mm}$ for the case $\sigma = R$. Any blue curve represents the original signal, while the red and green curves give the low-pass and high-pass components, respectively. The black dotted lines display the fitting curves of the high-(low-) pass components by an exponentially damping sinusoid, with the best-fit periods and damping times shown in each panel. Middle column: same as the left but for $\sigma = 0.5R$. Right column: same as the left but for $\sigma = 2R$.

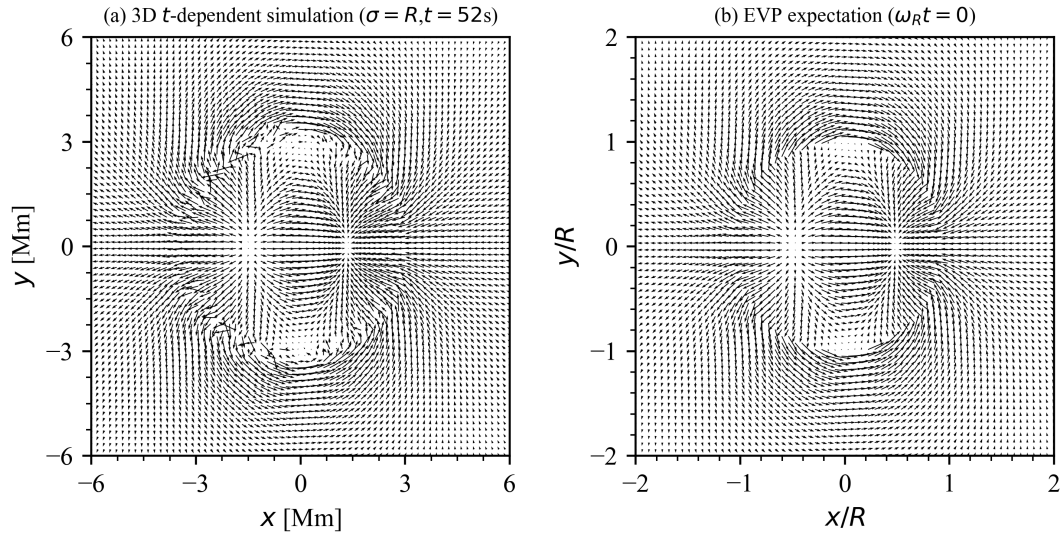


Figure 7. Velocity fields in the apex plane of (a) the simulated short-period component at some representative instant and (b) the eigenvalue problem expectation for the first leaky kink mode.